Electronic Supplementary Information for

Negatively charged platinum nanoparticles on dititanium oxide electride for ultra-durable electrocatalytic oxygen reduction

Erbing Hua,‡[a] Seunggun Choi,‡[b] Siyuan Ren,‡[a] Sungjun Kim,[c] Ghulam Ali,[d] Seon Je Kim,[a] Woo-Sung Jang,[a] Soyun Joo,[e] Jingshu Zhang,[e] Seulgi Ji,[f] Yun Seong Cho,[g] Joohoon Kang,[g] Taeseup Song,[b] Seungbum Hong,[e] Heechae Choi,[f,h] Young-Min Kim,[a] Hyuksu Han*[i] and Sung Wng Kim*[a]

[a]Department of Energy Science, Sungkyunkwan University; Suwon 16419, Republic of Korea.

[b]Department of Energy Engineering, Hanyang University; Seoul 04763, Republic of Korea.

[c]Hydrogen Energy Research Center, Korea Research Institute of Chemical Technology; Daejeon, Republic of Korea.

[d]U.S.-Pakistan Center for Advanced Studies in Energy (USPCASE), National University of Sciences and Technology (NUST), Sector H-12, Islamabad, Pakistan.

[e]Department of Materials Science and Engineering, KAIST; Daejeon, Republic of Korea.

[f]Institute of Inorganic Chemistry, University of Cologne, Greinstr. 6, 50939, Cologne, Germany.

[g]School of Advanced Materials Science and Engineering, Sungkyunkwan University; Suwon 16419, Republic of Korea.

[h]Department of Chemistry, Xi'an Jiaotong-Liverpool University, Suzhou, Jiangsu, 215123, China.

[i]Department of Energy Engineering, Konkuk University; Seoul 05029, Republic of Korea.

‡These authors contributed equally to this work

*Email: hhan@konkuk.ac.kr (H.H.) and kimsungwng@skku.edu (S.W.K.)

Supplementary Experimental

Synthesis of $[Ti_2O]^{2+}\cdot 2e^-$ electride

All synthetic part were operated in glove boxes filled with high-purity argon gas (Ar 99.999%) to minimize the oxidation of raw materials and synthesized samples. Stoichiometric polycrystalline $[Ti_2O]^{2+}\cdot 2e^-$ electrides were synthesized by the arc melting method under high-purity Ar atmosphere. We mixed Ti powder (Alfa Aesar; 99.98%) and TiO_2 in a 2:1 molar ratio of Ti to O. To collect homogeneous and single phase of $[Ti_2O]^{2+}\cdot 2e^-$ electrides via the arc melting method, mixed powder was pelletized under 20 MPa. The pellets were melted in the Ar-filled arc melting chamber over 2000 °C and remelted to fabricate polycrystalline coin-shaped $[Ti_2O]^{2+}\cdot 2e^-$ electride samples. Coin-shaped polycrystals were pulverized for structural characterization and used as the working electrode in electrochemical experiments.

Synthesis of ea-Pt/a-TiO_X/$[Ti_2O]^{2+}\cdot 2e^-$

The deposition of Pt NPs onto Ti_2O was conducted by wet-chemical infiltration methods in combination with *in situ* electrochemical reduction process.[1] 5 mg of the pulverized Ti_2O powder was dipped into the 353 μL of aqueous 8 mM $PtCl_4$ (Sigma Aldrich; 98%) solution. Pt/Ti_2O was obtained after the evaporation of the water solvent in vacuum oven at 80 °C. Electrochemical activation process was then performed by applying continuous potential of 0.4 V vs. reversible hydrogen electrode (RHE) for 1 h using a potentio station, leading to the complete reduction of $PtCl_4$ and the formation of negatively charged Pt NPs on the $[Ti_2O]^{2+}\cdot 2e^-$ electride surface.

Structural characterization by XRD

The crystal structure was investigated by XRD using a Rigaku SmartLab diffractometer with monochromatic Cu K_α radiation (8.04 keV) at room temperature. The well-ground powder samples were prepared in glove boxes and measured in a plastic dome-type stage filled with Ar gas to avoid oxidation during measurements. General Structure Analysis System (GSAS) software package was applied to perform Rietveld refinement. To confirm the effect of oxidation to the crystal structure of the $[Ti_2O]^{2+}\cdot 2e^-$ electride, we prepared unoxidized powder handled in Ar-filled glove boxes and oxidized powder neglected in the air and water over 3 months. Then, the same XRD measurement procedures were conducted for each sample. The Ar-exposed sample was prepared in glove boxes filled with high-purity Ar gas by cutting and pulverizing to make fresh surfaces.

Electrical transport measurements and characterization

The resistivity and Hall effect measurements were performed to confirm the oxidation effects on the electrical properties. Three different samples, which are cleaved in the glove boxes (UHV-cleaved), exposed to air for 1 month (air-exposed), and immersed in the water for 1 month (water-exposed), were prepared and Au was deposited as electrodes with a thermal evaporator equipped in a glove box onto the surface of the samples to eliminate the noise from contact resistance with four-point and Hall bar configurations. After the contacts were made, Apiezon N grease was coated onto the sample surfaces to prevent further oxidation during measurements. The temperature-dependent resistivity and Hall effect measurements were performed by the physical property measurement system (PPMS DynaCool, Quantum Design). The carrier concentrations (N_H) were derived from the Hall coefficient (R_H). The measured sample in the inset of Fig. S28b was prepared in a glove box filled with high-purity Ar gas by cleaving and polishing to make a fresh surface.

Photoemission spectroscopy measurements and characterization

A XPS and UPS measurements were performed to investigate chemical and electronic states of $[Ti_2O]^{2+}\cdot 2e^-$ electride surface. To investigate into the as-prepared bulk information and avoid the disturbance of surface species, we cleaved the shiny surface of the $[Ti_2O]^{2+}\cdot 2e^-$ electride (air-exposed sample) with Argon (Ar) plasma sputtering was operated under maximum power for 12 hours to remove the surface substance on as-prepared samples (4 mm × 4 mm × 0.5 mm shiny plate), under ultrahigh vacuum (UHV) conditions (~10^{-10} torr) with a post attached Torr Seal before photoemission spectroscopy measurements. Then, the measurement was carried out under a vacuum of ca. 3×10^{-10} torr. The photoemission results were obtained using a Scienta R4000 electron analyzer with an Al K_α X-ray source (1486.7 eV) and a discharge lamp that emitted an excitation line of He I_α (21.2 eV). Core spectra of Ti 2*p* and O 1*s* were measured for analysis, and all spectra were fitted by comparing the binding energies of the component peaks with CasaXPS. Every peak was calibrated by the spectrum of hydrocarbon on the sample and reference Au attached next to the sample. In the work function (ϕ) measurement with UPS, the negative bias voltage of 1 kV was applied to clarify that the vacuum level of the sample exceeds that of an electron analyzer. Pt 4*f* XPS spectra was also mesaured for Pt/a-TiO_x/$[Ti_2O]^{2+}\cdot 2e^-$ and ea-Pt/a-TiO_x/$[Ti_2O]^{2+}\cdot 2e^-$ samples.

Atomic-scale transmission electron microscopy

TEM experiments were performed using a Cs-corrected TEM (JEM-ARM200F, JEOL) equipped with a cold field emission source, operating at 200 kV. To prevent oxidation of the TEM sample, a single-tilt vacuum transfer holder (Model VTST-4006, Gatan) was used for TEM experiments (UHV-cleaved samples). TEM samples for HRTEM and EDX were prepared as powder cleaved from a single phase polycrystal in the high-purity Ar-filled glove boxes. Air-/water-exposed samples was collected from the samples exposed to air and water for 3 months and prepared the specimen for TEM in above glovebox. Dual-beam focused ion beam (AURIGA CrossBeam Workstation, Carl Zeiss) was also used to obtain atomic-scale STEM images and chemical EDX mapping data with JEOL-EDX in the STEM imaging mode, and each detector has an effective detection area of 100 mm^2. The sample drift during the acquisition was compensated by tracking the reference atom position assigned at the beginning of the acquisition.

X-ray absorption spectroscopy

Hard X-ray absorption spectroscopy (XAS) was performed using Si(111) double crystal monochromator at 1D beamline of Pohang accelerator spectroscopy (PAL) and 8C beamlines of the Pohang accelerator laboratory, South Korea. A double crystal monochromator (DCM) Si(111) was employed at 1D beamline and measurements were taken with a ring current of 300 mA. The harmonics of the incident X-ray beam were detuned by DCM. The energy was calibrated using reference metallic foils prior to measurements. The XAS data of samples were obtained in transmission mode using a Pt metallic foil as reference. The background removal, normalization, and Fourier transform of the obtained signals were processed in the ATHENA package.[2]

Inductively coupled plasma optical emission spectroscopy

Pt amount in the samples were measured by inductively coupled plasma-optical emission spectroscopy (ICP-OES, Thermo Scientific, iCAP6500 Duo). RF power was set as 1350 W and the wavelength was 214.423 nm.

Preparation of catalyst inks and electrodes

5 mg of the catalyst powders and 5 mg of super P (Thermo Scientific; 99%) were dispersed in a mixture of 0.5 mL of DI water and 0.44 mL of 2-propanol (Sigma Aldrich; 99%) containing 60 μL of Nafion 117 solution (Sigma Aldrich; ~5%) by sonicating and stirring for more than 30 min. 11.2 μL of the dispersed catalyst ink was loaded onto a glassy carbon electrode with a diameter of 5 mm resulting in a catalyst loading amount of approximately ~0.28 mg cm^{-2}. For comparison purpose, the benchmark commercial Pt/C (Sigma Aldrich; 20 wt.%) catalyst was also prepared using the identical recipe.

Electrochemical characterization

Aqueous 0.1 M KOH (Daejung; 93%) solution was implemented as an electrolyte under 50 sccm of O_2 purging. Typical three electrode cell controlled by an electrochemistry workstation (model Autolab PGSTAT; Metrohm) was used for all the electrochemical characterizations. Pt sheet and Ag|AgCl were used as counter and reference electrodes, respectively. A titration vessel of clear glass was used as a testing cell. A rotating disk electrode (RDE) was used for all electrochemical tests. The distance between working and reference electrodes was about 1 cm. Catalysts were stabilized over 100 cycles of cyclic voltammetry in the potential window, 0.05 – 1.18 V_{RHE}. LSV curves were then measured from 1.1 V_{RHE} to 0.4 V_{RHE} at a scan rate of 5 mV s^{-1} using 2,500 rpm. All polarization curves were iR-compensated using solution resistance (R_s) values measured by electrochemical impedance spectroscopy (EIS) over the frequency range of 0.1 – 100 kHz under open circuit voltage (OCP). For chronoamperometry test, carbon paper was used as a substrate where the catalysts was loaded with the same loading density, 0.28 mg cm^{-2}.

Pt electrochemical surface area (ECSA) and specific activity determination via cyclic voltamettry (CV)

CVs were conducted for the non-faradaic region (0.025 V_{RHE} – 1.225 V_{RHE}) in 0.1 M $HClO_4$ to calculate the ECSA of the samples. H adsorbs on the surface before the potential reaches 0 V_{RHE}. This is called hydrogen underpotential deposition (H_{upd}) which can be calculated by integrating CV data. Current by capacitance of the catalysts should be excluded when the integration is conducted. ECSA can be calculated by the following equation:

$$\mathrm{ECSA_{Pt,cat}}(\mathrm{m^2\,g_{Pt}^{-1}}) = \left(\frac{\mathrm{Q_{H-adsorption}(C)}}{210\ \mu\mathrm{C\ cm_{Pt}^{-2}}\ \mathrm{L_{Pt}(mg_{Pt}cm^{-2})A_g(cm^2)}}\right)10^5$$

where $ECSA_{Pt,cat}$ is ECSA of the corresponding sample, $Q_{H\text{-adsorption}}$ is the hydrogen adsorption charge, L_{Pt} is Pt mass loading, and A_g is the geometrical surface area of the electrode. Assumption that H atoms are adsorbed on only Pt atoms was made here. Conversion factor Q_H = 210 μC cm^{-2} is the charge of full coverage for clean polycrystalline Pt.[3] Specific activity is calculated determined via the following equation:

$$\mathrm{Specific\,activity(mA\,cm_{Pt}^{-2})} = \left(\frac{\mathrm{Current\ density\ (mA\,cm^{-2})}}{\mathrm{ECSA_{Pt,cat}(m^2 g_{Pt}^{-1})L_{Pt}\,(mg_{Pt}\,cm^{-2})}}\right)10^{-1}$$

Calculation of mass activity

When calculating mass activity, the kinetic current was used due to mass-transport correction for thin-film RDEs:[4]

$$\mathrm{I_k(A)} = \left(\frac{\mathrm{I_{lim}(A) \times I(A)}}{\mathrm{I_{lim} - I}}\right)$$

where I_k is the kinetic current. I_{lim} is the measured limiting current which is the current at 0.4 V_{RHE} in our research. I is the current at the specified potential. 0.9 V_{RHE} is used in the usual case. The mass activity was calculated by the following equation:[5]

$$\text{Mass activity}(\text{A mg}_{\text{Pt}}^{-1}) = \left(\frac{I_k(\text{A})}{L_{Pt}(\text{mg}_{Pt}\text{cm}^{-2})A_g(\text{cm}^2)} \right)$$

However, mass activity determined by the equation above is not suitable to analyze the activity under a wide range of potential as in Fig. 3b. Therefore, mass activity in Fig. 3b was calculated by the following equation:

$$\text{Mass activity}(\text{A mg}_{\text{Pt}}^{-1}) = \left(\frac{\text{Current density (mA cm}^{-2})}{L_{Pt}(\text{mg}_{Pt}\,\text{cm}^{-2})} \right)^{3} \times 10$$

Calcualtion of charge transfer number (n)

The electrons transferred number in the ORR can be measured by well-known Koutecky-Levich (K-L) equation:

$$\frac{1}{J} = \frac{1}{J_L} + \frac{1}{J_K} = \frac{1}{B\omega^{1/2}} + \frac{1}{J_K}$$

$$B = 0.62nFC_0(D_0)^{2/3}\nu^{1/6}$$

in which J stands for the measured current density, J_L and J_K denote the diffusion-limiting current density and the kinetic-limiting current density, respectively.[6] B represents the slope of the K-L plots and "ω" is the RDE rotation rate, which is equal to 2πN (N: linear rotation speed). 'n' is the number of electrons involved in ORR, 'F' is the Faraday constant (96,485 C mol^{-1}), "C_0" is the bulk concentration of O_2 (1.2×10^{-3} mol L^{-1}), 'D_0' is the diffusion coefficient of O_2 (1.9×10^{-5} cm s^{-1}) in 0.1 M KOH electrolyte, and ν is the kinematic viscosity of the electrolyte (0.1 m^2 s^{-1}) in 0.1 M KOH electrolyte.

Calculation of electrocial double layer capacitance

Electrochemical double-layer capacitance (C_{dl}) was estimated by measuring CV scans in N_2-saturated 0.1 M KOH soultion at the potential range where at only non-Faradaic current generates (i.e., 0.2 – 0.3 V_{RHE}). CV scans were conducted at scan rates 20, 40, 60, and 80 mV s^{-1} over the voltage range. The difference in current density between the anodic and cathodic sweeps ($J_{anodic} - J_{cathodic}$) at the mid potential of 0.15 V_{RHE} was plotted as a function of the scan rate in which the slope corresponds to twice the C_{dl} of the catalyst.[7]

Preparation of the MEAs and single-cell tests

The MEAs for AEMFC was prepared by a catalyst-coated membrane (CCM) method. Prior to catalyst layer coating process, the QPC-TMA[8] membranes (50 μm) were converted into hydroxide forms by immersing them in a 1.0 M KOH aqueous solution for 2 h, followed by rinsing with deionized water. Commercial 60 wt.% PtRu/C (Alfa Aesar) and the prepared 0.7 wt.% catalyst powder were used as anode and cathode catalyst, respectively. Catalyst slurries were prepared by mixing the catalysts with a QPC-TMA ionomer (5 wt.% ionomer in n-propanol aqueous solution, the ionomer to support weight ratio were 0.5 for anode, and 0.4 for cathode, respectively) in an aqueous solution of isopropyl alcohol. To obtain homogeneous dispersion, each catalyst slurry was ultrasonicated for more than 30 min. The prepared slurries were directly sprayed onto the membranes to fabricate catalyst layers. The catalytic material loading was 0.4 mg_{PtRu} cm^{-2} for anode, and 0.01 mg_{Pt} cm^{-2} for cathode, respectively. The active area of the MEAs were 5 cm^2. Prior to the single-cell application, the CCM was immersed in a 1.0 M KOH aqueous solution for 1 h to convert the QPC-TMA ionomer into a hydroxide form and rinsing with deionized water. Afterward, the CCM was sandwiched between two gas

diffusion layers with microporous layer (JNT-30-A6H, JNTG Co.) without a hot-pressing process. For benchmarking, the MEAs with commercial 20 wt.% Pt/C (Alfa Aesar) was also prepared by using the same fabrication process (Table S5 and S6). To evaluate the AEMFC performance of the prepared MEAs, each MEA was inserted between two graphite plates with a one-channel serpentine-type flow field (2.2 cm x 2.3 cm). Single cell was assembled by applying torque (8.5 N m) to each screw of the end plates and connected to a fuel cell test station (CNL Energy). To evaluate the AEMFC performance of the MEAs, humidified hydrogen and oxygen were fed to the anode and the cathode at constant flow rates of 0.8 and 1.1 L min^{-1}, respectively. The temperature of the single cell was fixed at 60 °C, and the dew points of the hydrogen and oxygen gases were maintained at 56 and 58 °C, respectively. The AEMFC performance was evaluated under the above condition until the stabilized cell voltage was achieved at the corresponding discharge current.

Computational methods

All density functional theory (DFT) calculations were carried out using the Vienna ab initio package (VASP) with the projector augmented wave method (PAW) to describe interaction between valence and core electrons.[9–11] The general gradient approximation (GGA) with the Perdew, Burke and Ernzehof (PBE) was employed for the plane-basis wave expansion.[12] The optimization of cell parameters and kinetic energy cut-off of 400 eV was used.[13] The energy convergence criteria in the self-consistent field were set to 10^{-4} eV. All geometry structures were fully relaxed until Hellman-Feynman forces achieved a range of 0.1 eV $Å^{-1}$. The supercell dimensions for Pt NPs slab, consisting of 64 atoms, are 11.25 × 11.25 × 27.25 Å, and to avoid the interactions between the adjacent periodic supercells, the vacuum layers were placed along the c axis enough. The charged Pt (111) slab was optimized by adding excess electrons to the neutral Pt (111) slab, in which the number of electrons derived from the calculated density of states (DOS) of the neutral Pt (111) slab (Fig. S27). By considering the previous literature,[14] we calculated the number of excess electrons on the Pt (111) from the difference between work function values of Pt metal and the negatively charged our Pt NPs, which was set to be around 1.0 eV in the present work (Fig. S26). In a simple manner, the number of excess electrons were extracted by the integral of the green area in the density of state, which gives 0.27e^- per one Pt atom at the surface.

Oxygen reduction reaction via the four electrons pathway on Pt NPs under alkaline condition (pH = 13) undergoes as follows,

(i) $O_2\ (g) + * \rightarrow O_2*$

(ii) $O_2* + H_2O\ (l) + e^- \rightarrow HOO* + OH^-$

(iii) $HOO* + e^- \rightarrow O* + OH^-$

(iv) $O* + H_2O(l) + e^- \rightarrow HO* + OH^-$

(v) $HO* + e^- \rightarrow OH^- + *$

The Gibbs free energies of adsorbates (ΔGG) were obtained using the following equation,

$$\Delta GG = \Delta EE_{aaaaaa} + \Delta EE_{ZZZZZZ} - TT\Delta SS + \Delta GG_{UU} + \Delta GG_{pppp}$$

where ΔEE_{aaaaaa}, ΔEE_{ZZZZZZ}, T and ΔSS represent the adsorption energy derived from DFT calculations, difference in zero-point energies, the temperature at 300 K, and the changes of entropies, respectively. ΔGG_{UU} is $-$neU, where n, e and U are the number of transferred electrons, the transferred charge and U is the applied voltage. ΔGG_{pppp} is relative to $-kk_{BB}TTTTT10 \times pppp$, where kk_{BB} is the Boltzmann constant. Noted that for ΔGG calculations of four electrons pathway in ORR, the final reaction step was set as zero.

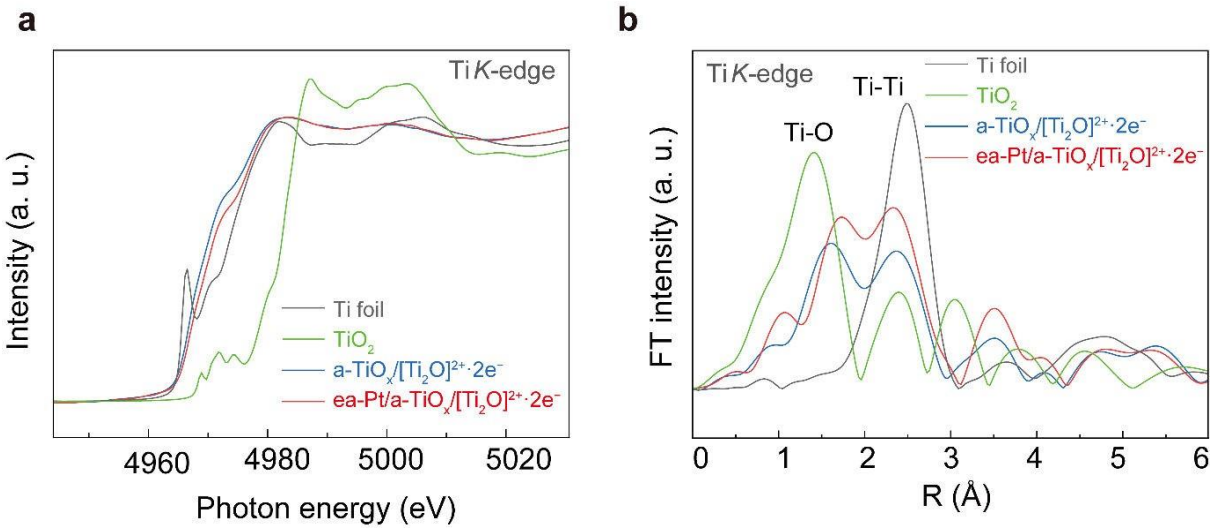

Fig. S1 Comparison between different Ti at the Ti *K*-edge spectra. (a) X-ray absorption near-edge spectroscopy (XANES) and (b) extended X-ray absorption fine structure (EXAFS) of a-$TiO_x/[Ti_2O]^{2+}\cdot 2e^-$ and ea-Pt/a-$TiO_x/[Ti_2O]^{2+}\cdot 2e^-$ at Ti *K*-edge.

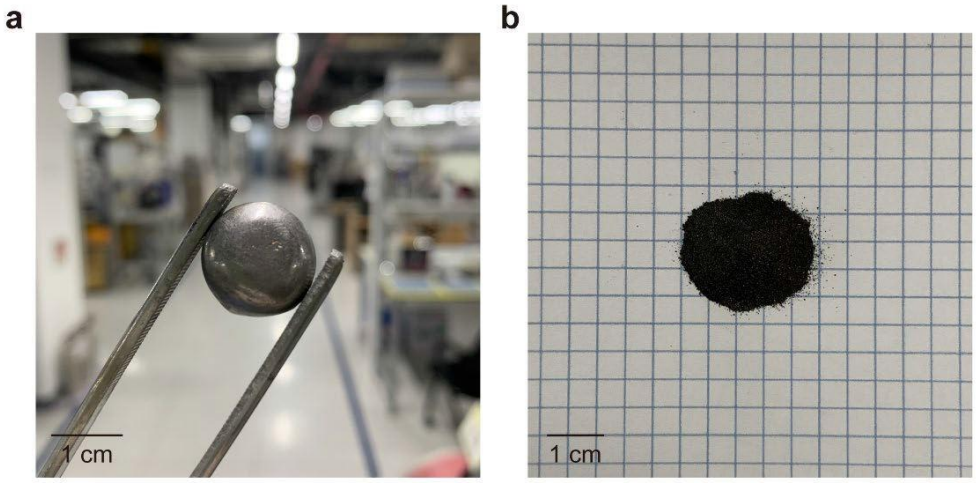

Fig. S2 Air-stable $[Ti_2O]^{2+}\cdot 2e^-$ electride. (a) Air-exposed $[Ti_2O]^{2+}\cdot 2e^-$ bulk. (b) Pulverized powders of $[Ti_2O]^{2+}\cdot 2e^-$ in air.

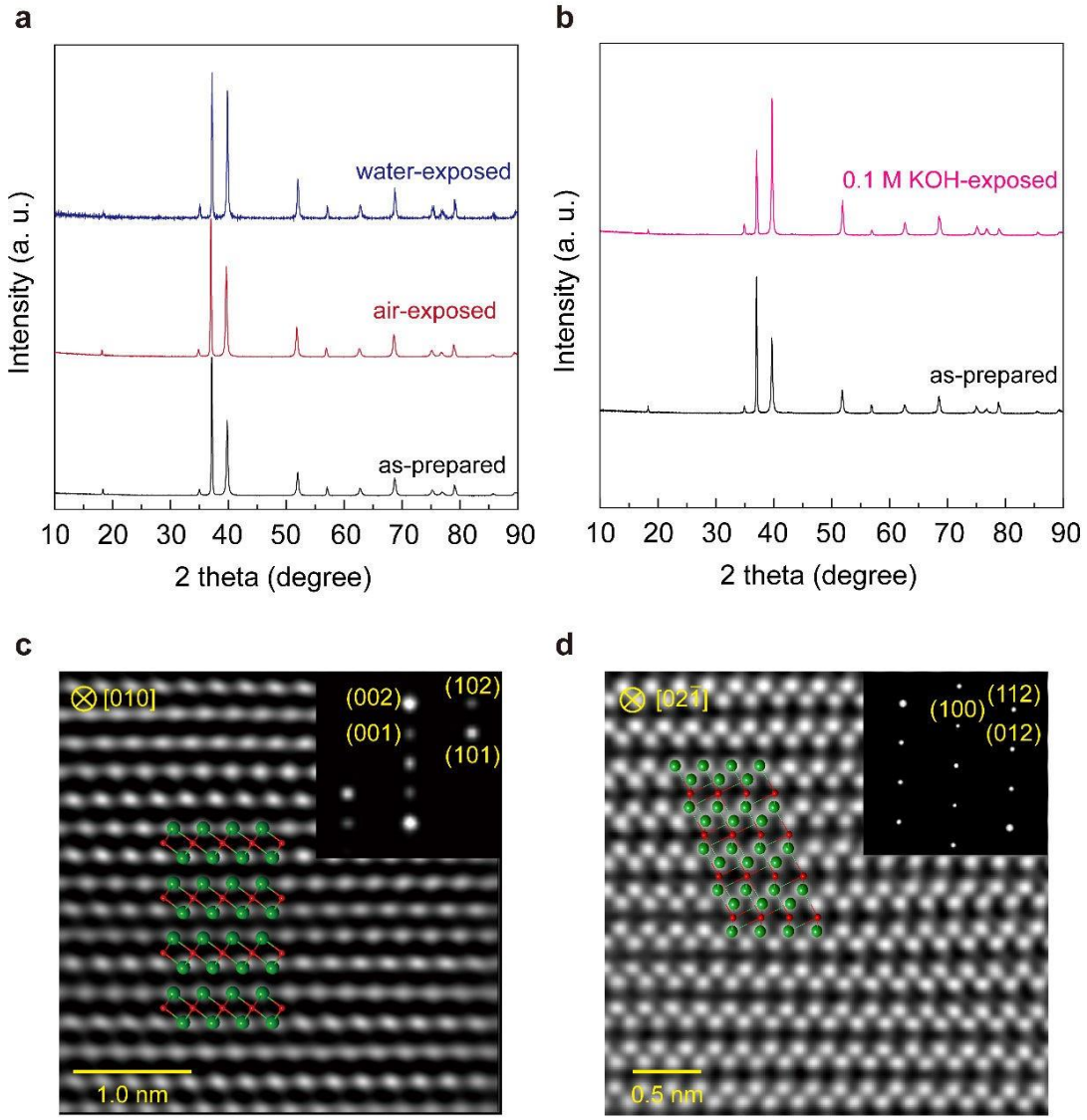

Fig. S3 Chemical stability and atomic structure of $[Ti_2O]^{2+}\cdot 2e^-$ electride. (a) Powder XRD patterns of as-prepared (black), air-exposed (red), and water-exposed (blue) $[Ti_2O]^{2+}\cdot 2e^-$. (b) Powder XRD patterns of as-prepared (black) and 1.0 M KOH-exposed (pink) $[Ti_2O]^{2+}\cdot 2e^-$. (c), (d) Atomic-scale high-angle annular dark-field STEM. The corresponding crystal structures are superimposed on the observed images.

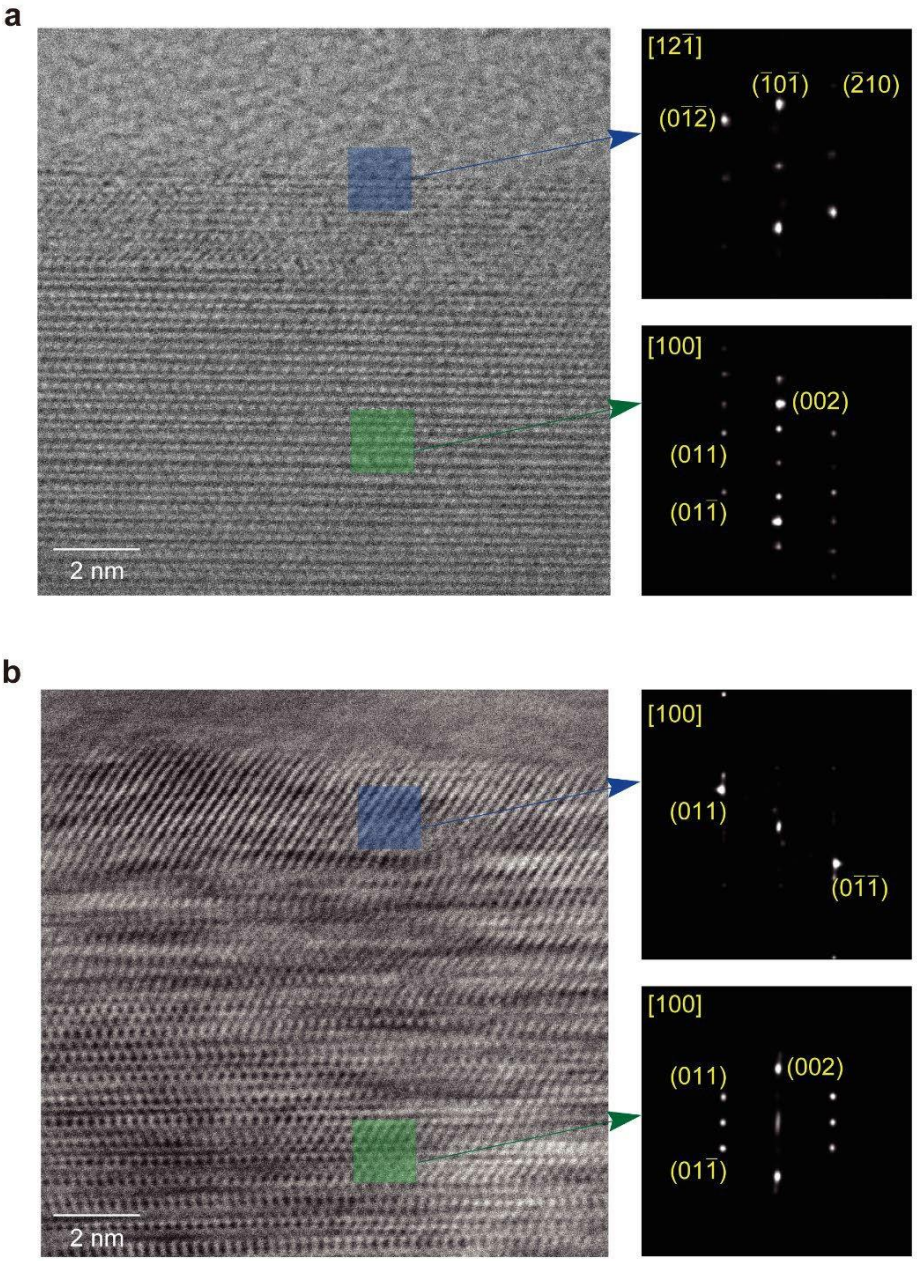

Fig. S4 Surface structure of as-cleaved $[Ti_2O]^{2+}\cdot 2e^-$ electride. (a), (b) HR-STEM image of as-cleaved $[Ti_2O]^{2+}\cdot 2e^-$ (left) and corresponding diffraction patterns of surface (right top, blue box) and bulk crystal (right bottom, green box) regions. Two differenct regions in the identical sample were analyzed and presented as (a) and (b).

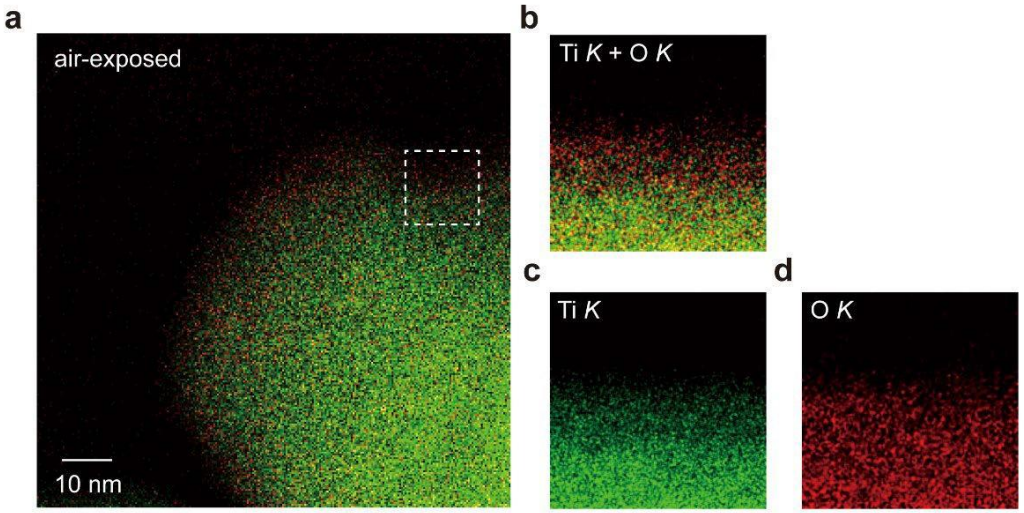

Fig. S5 Surface structure of air-exposed $[Ti_2O]^{2+}\cdot 2e^-$ electride. (a) STEM-EDX elemental mapping image of air-exposed $[Ti_2O]^{2+}\cdot 2e^-$, which is composed of Ti *K* (green) and O *K* (red) signals. (b) Combined image of Ti *K* and O *K* signals of the white dashed region in (a). (c), (d) Seperated images of (c) Ti *K* and (d) O *K* sigmals from (b).

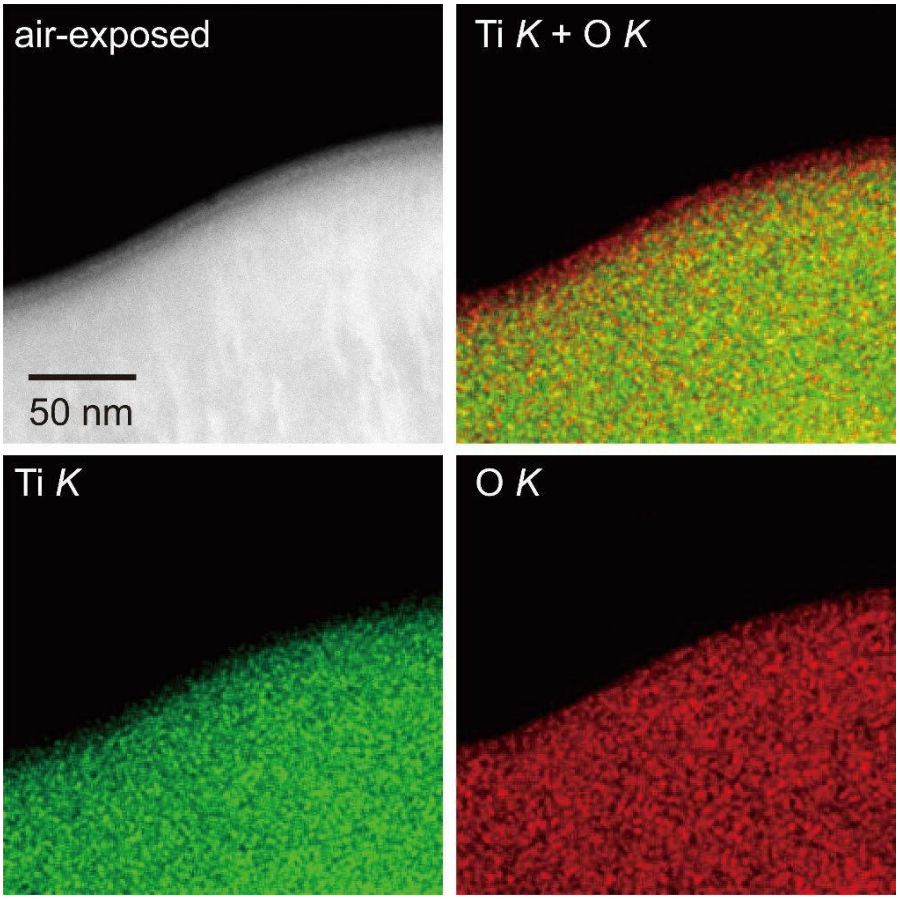

Fig. S6 HR-TEM image and STEM-EDX elemental mapping of air-exposed $[Ti_2O]^{2+}\cdot 2e^-$, which is composed of Ti K (green) and O K (red) signals.

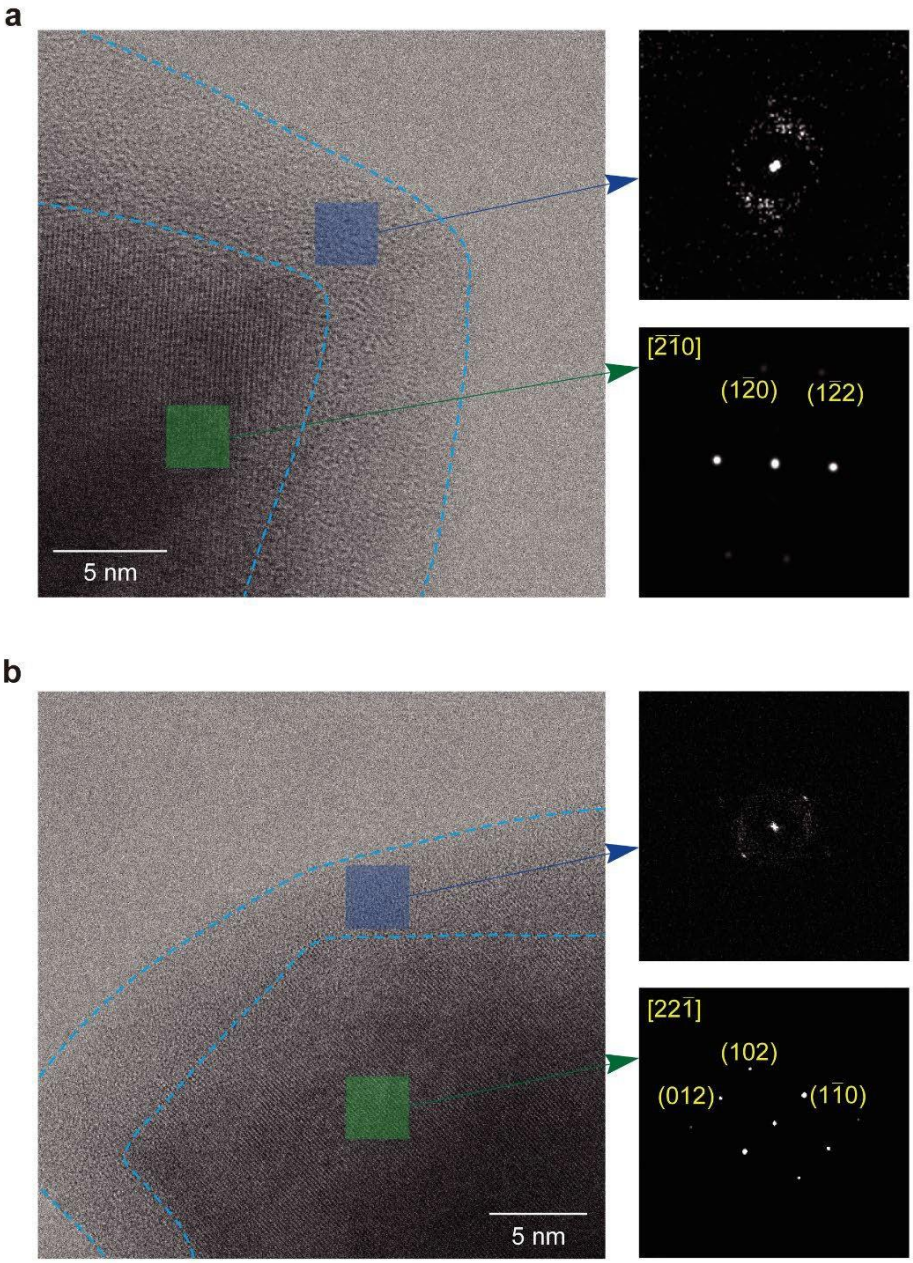

Fig. S7 Surface structure of water-exposed $[Ti_2O]^{2+}\cdot 2e^-$ electride. (a), (b) HR-STEM image of water-exposed $[Ti_2O]^{2+}\cdot 2e^-$ (left) and corresponding diffraction patterns of surface amorphous (right top, blue box) and bulk crystal (right bottom, green box) regions. Two differenct regions in the identical sample were analyzed and presented as (a) and (b).

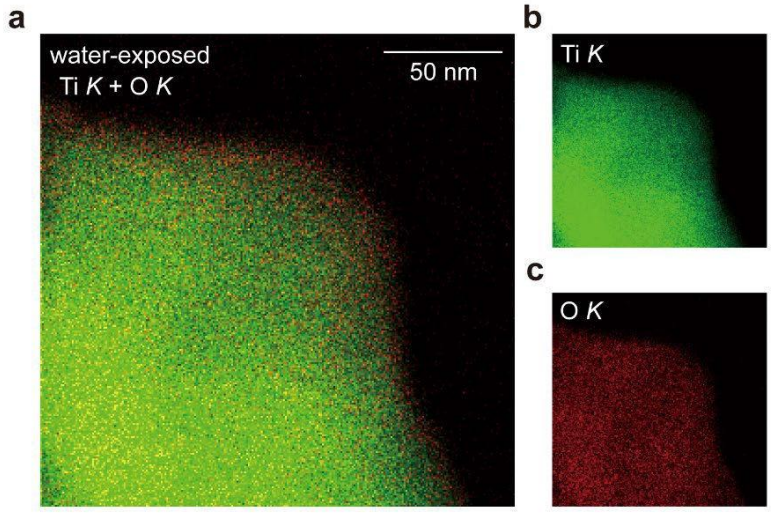

Fig. S8 Surface structure of water-exposed $[Ti_2O]^{2+}\cdot 2e^-$ electride. (a), (b), (c) STEM-EDX elemental mapping of water-exposed $[Ti_2O]^{2+}\cdot 2e^-$ (a), which is composed of (b) Ti *K* (green) and (c) O *K* (red) signals.

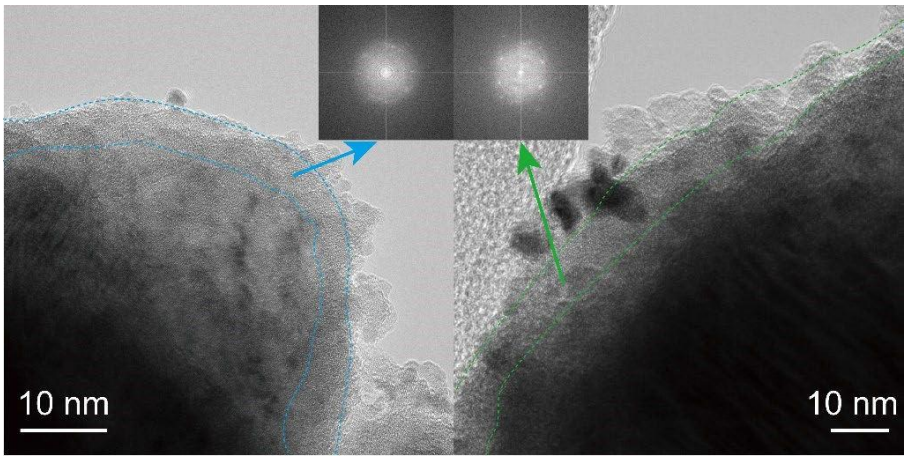

Fig. S9 HRTEM image of ea-Pt/a-TiO_x/$[Ti_2O]^{2+}\cdot 2e^-$ and corresponding diffraction patterns of surface amorphous regions.

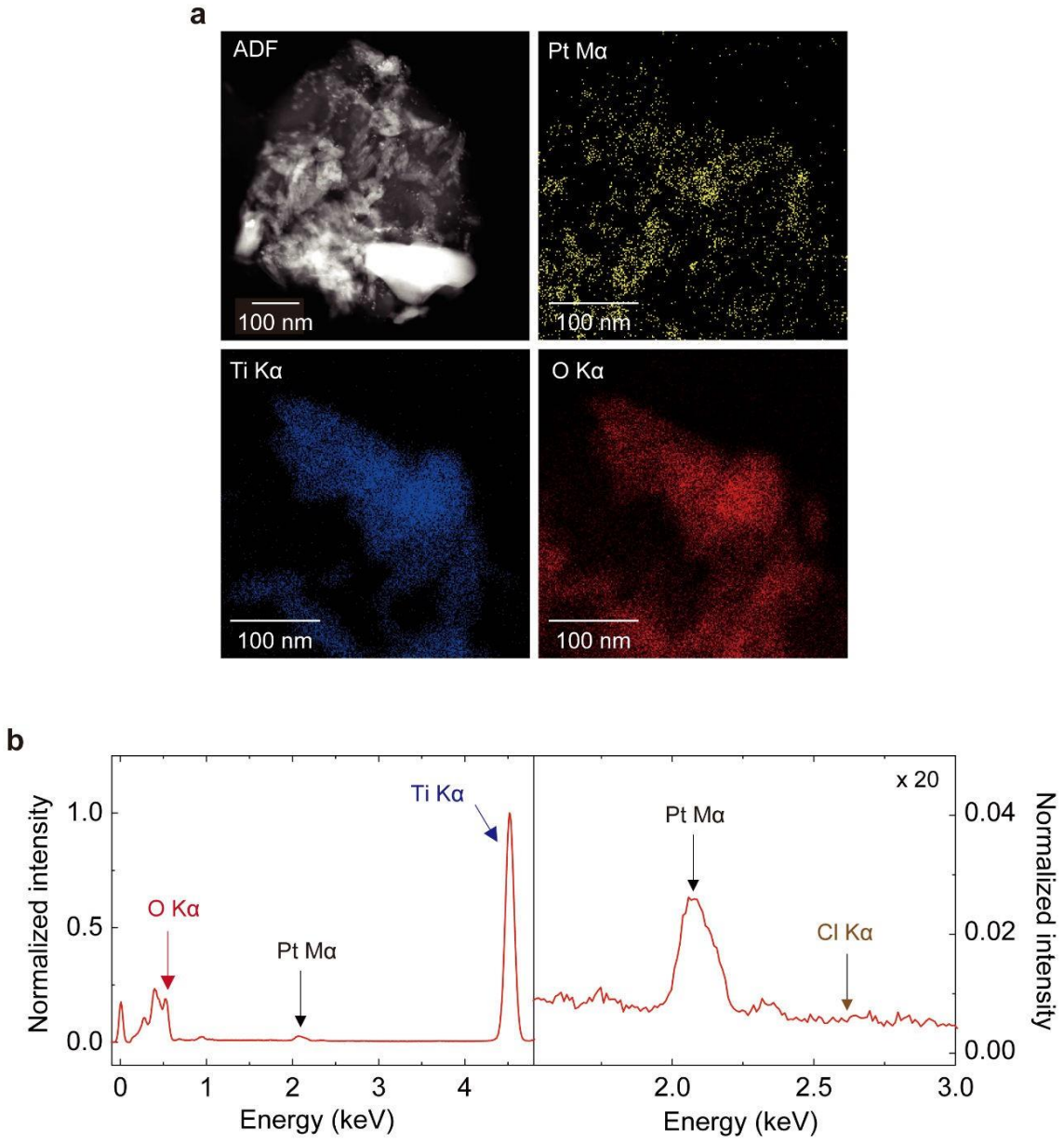

Fig. S10 EDX mapping of ea-Pt/a-TiO_x/$[Ti_2O]^{2+}\cdot 2e^-$. (a) STEM-EDX elemental mapping images of ea-Pt/a-TiO_x/$[Ti_2O]^{2+}\cdot 2e^-$. (b) Corresponding EDX spectra.

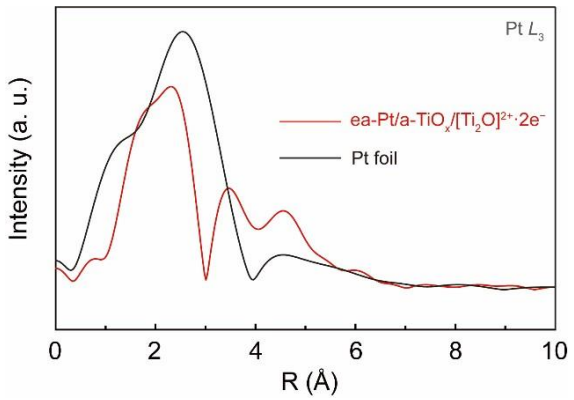

Fig. S11 Extended X-ray absorption fine structure (EXAFS) of ea-Pt/a-TiO_x/$[Ti_2O]^{2+}$·$2e^-$ at Pt L_3-edge.

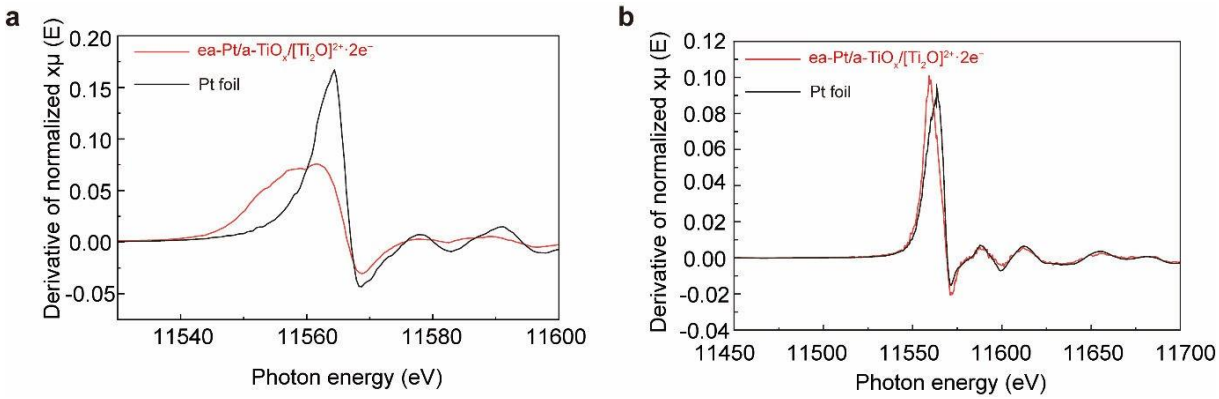

Fig. S12 Derivatives of normalized intensity at Pt *L*-edge measured at different beam line, (a) 1D KIST-PAL and (b) 8C beamlines of the Pohang accelerator laboratory.

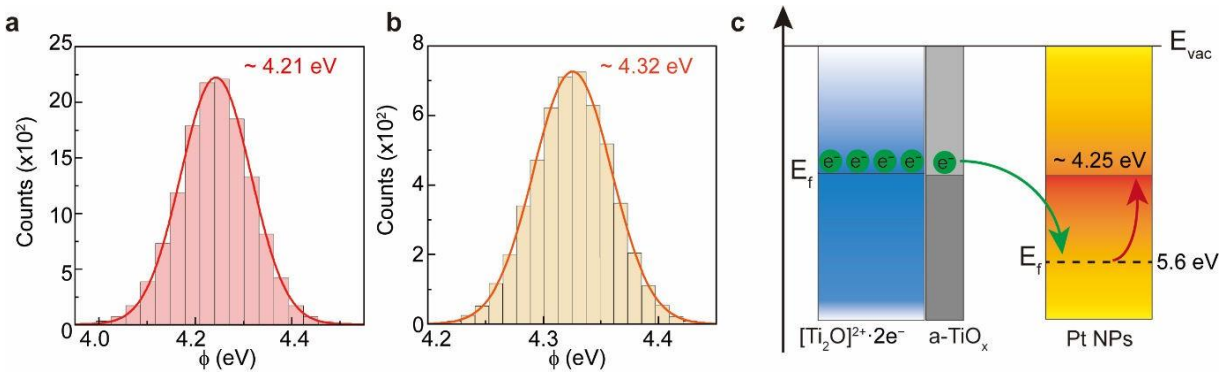

Fig. S13 Measurement of the work function by KPFM. (a) Work function value of $[Ti_2O]^{2+}\cdot 2e^-$ sample. (b) Work function value of a-TiO_x/$[Ti_2O]^{2+}\cdot 2e^-$ sample. (c) Schematic illustration of band alignment due to the charge transfer for the negatively charged Pt NPs on the surface of a-TiO_x/$[Ti_2O]^{2+}\cdot 2e^-$.

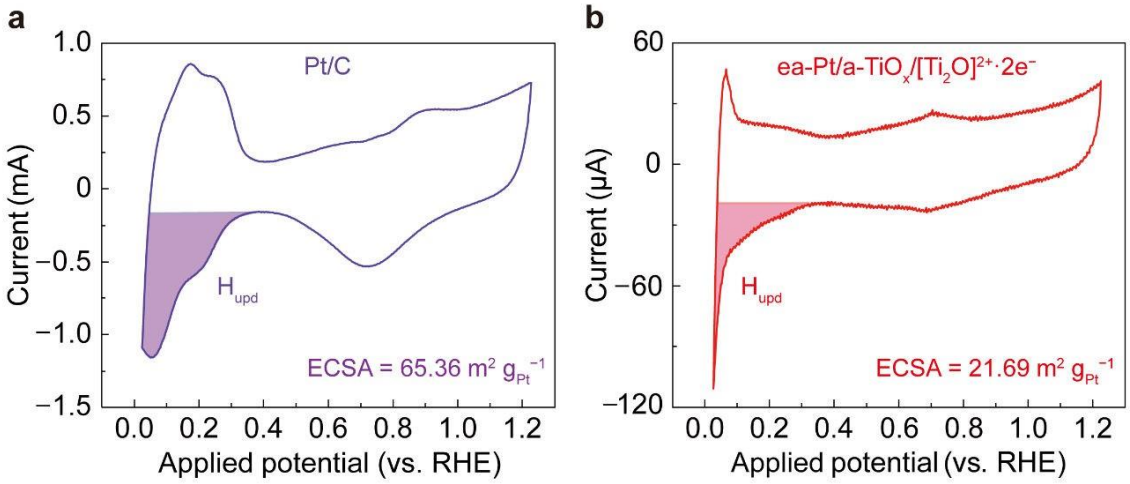

Fig. S14 Electrochemical surface area (ECSA) determination. (a) Cyclic voltammetry (CV) curves for commercial Pt/C measured in N_2-saturated 0.1 M $HClO_4$ solution using a scan rate of 5 mV s^{-1} and the rotating speed of 1,600 rpm. (b) ea-Pt/a-TiO_x/$[Ti_2O]^{2+}$·$2e^-$ catalysts measured under the same condition.

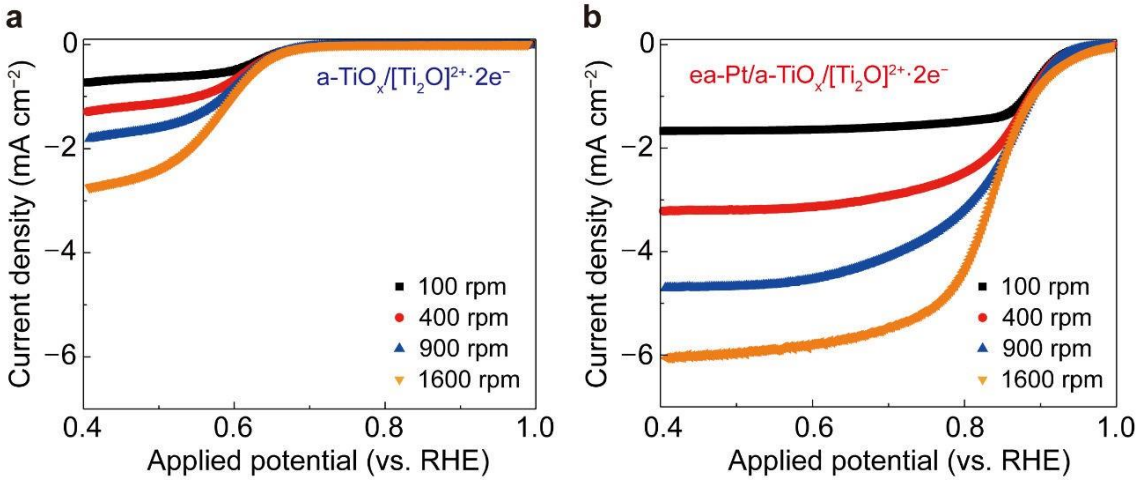

Fig. S15 ORR LSV polarization curves. (a) ORR LSV polarization curves for a-TiO_x/$[Ti_2O]^{2+}$·$2e^-$ catalysts measured in O_2-saturated 0.1 M KOH with different rotating speeds at a scan rate of 5 mV s^{-1}. (b) ea-Pt/a-TiO_x/$[Ti_2O]^{2+}$·$2e^-$ catalysts measured under the same conditions.

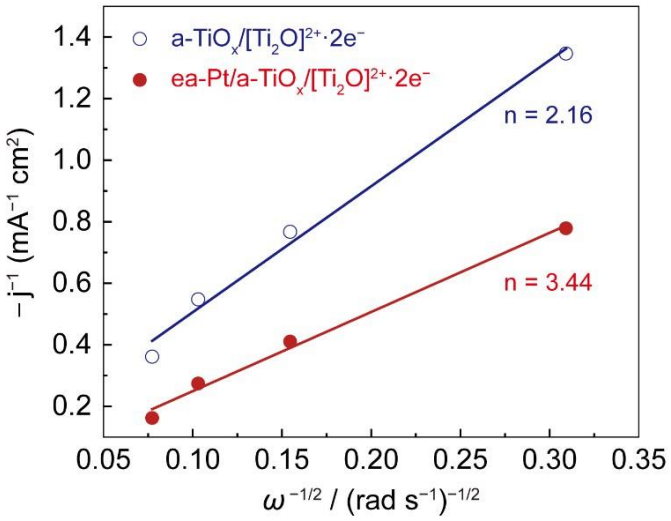

Fig. S16 Estimation of charge transfer number for ORR. Koutecky-Levich plots of a-$TiO_x/[Ti_2O]^{2+}\cdot 2e^-$ and ea-Pt/a-$TiO_x/[Ti_2O]^{2+}\cdot 2e^-$ catalysts at an electrode potential of 0.4 V vs. RHE.

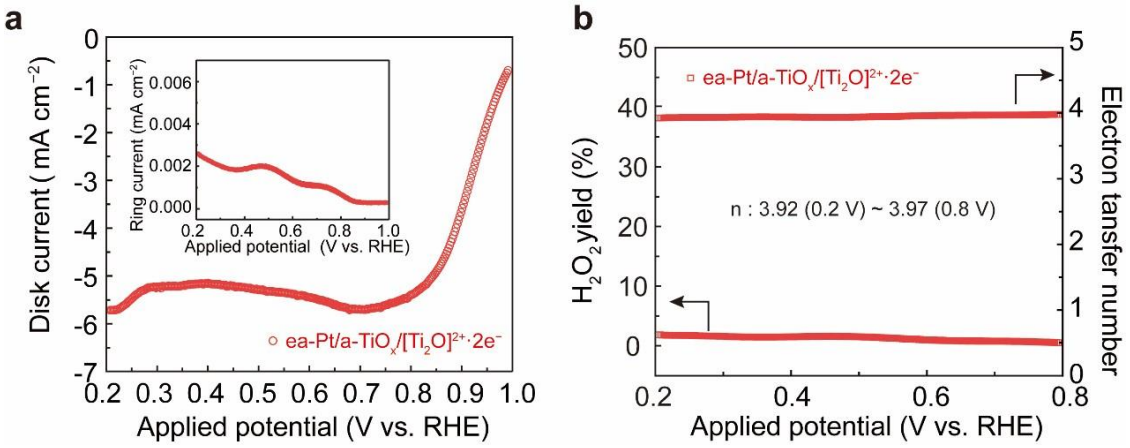

Fig. S17 Measurement of the electron transfer number for ORR. (a) Disk and ring (inset) currents measured by using RRDE for ORR in 0.1 M KOH. (b) Calculated charge transfer number and H_2O_2 yield for the ea-Pt/a-TiO$_x$/$[Ti_2O]^{2+}$·2e$^-$.

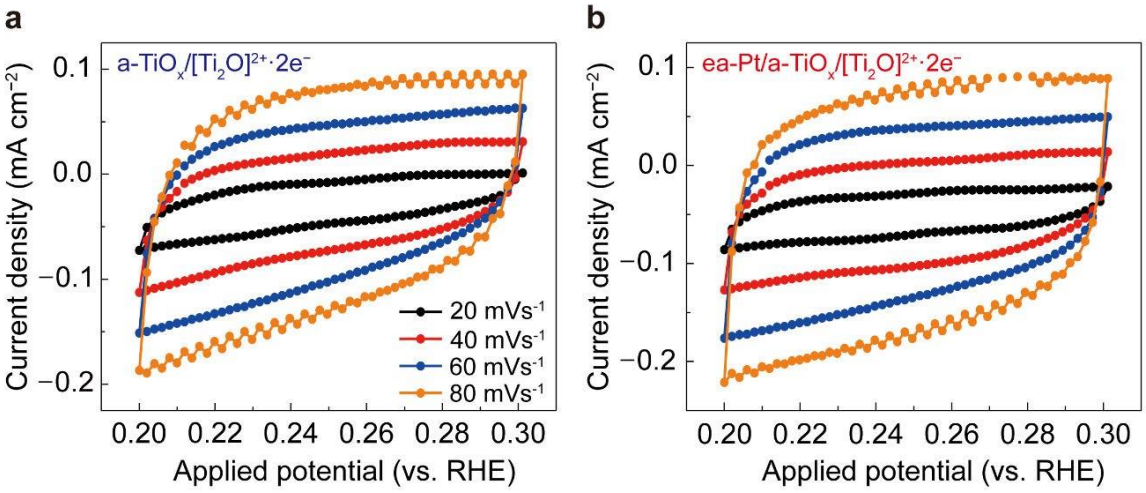

Fig. S18 Electrical double layer capacitance measurement. (a) CV curves for a-TiO_x/$[Ti_2O]^{2+}$·$2e^-$ catalysts measured in a capacitive current region (0.20 – 0.30 V_{RHE}) at scan rates of 20, 40, 60, and 80 mV s^{-1} in N_2-saturated 0.1 M KOH electrolyte. (b) ea-Pt/a-TiO_x/$[Ti_2O]^{2+}$·$2e^-$ catalysts measured under the same conditions.

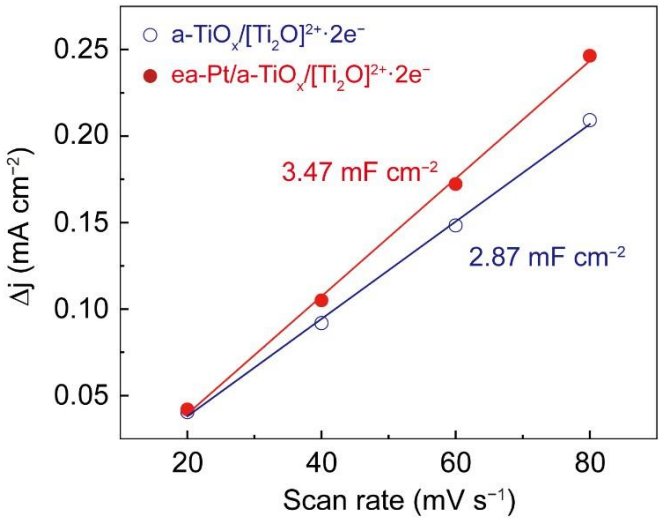

Fig. S19 Electrical double layer capacitance measurement. Electrical double layer capacitance measurement for a-$TiO_x/[Ti_2O]^{2+}\cdot 2e^-$ and ea-Pt/a-$TiO_x/[Ti_2O]^{2+}\cdot 2e^-$ catalysts. Plots (solid lines) of current difference between anodic and cathodic sweep as a function of scan rate correspond to the values of C_{dl}.

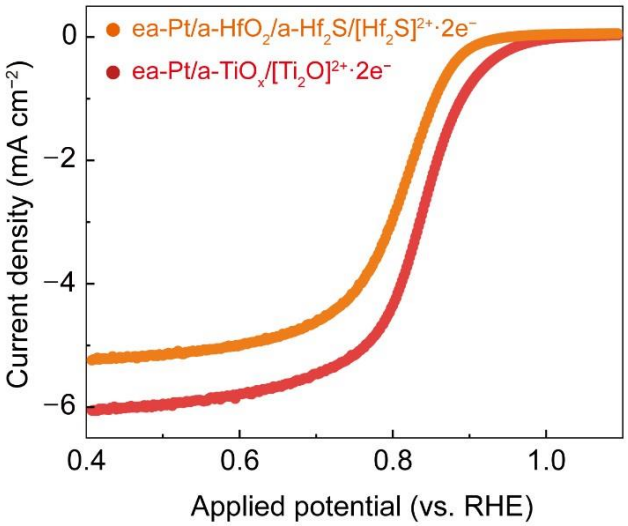

Fig. S20 ORR polarization curves of Pt NPs supported by electrides. The ea-Pt/a-HfO_2/a-$Hf_2S/[Hf_2S]^{2+}\cdot 2e^-$ (orange) and the ea-Pt/a-$TiO_x/[Ti_2O]^{2+}\cdot 2e^-$ (red) measured in 0.1 M KOH using a scan rate of 5 mV s^{-1}.

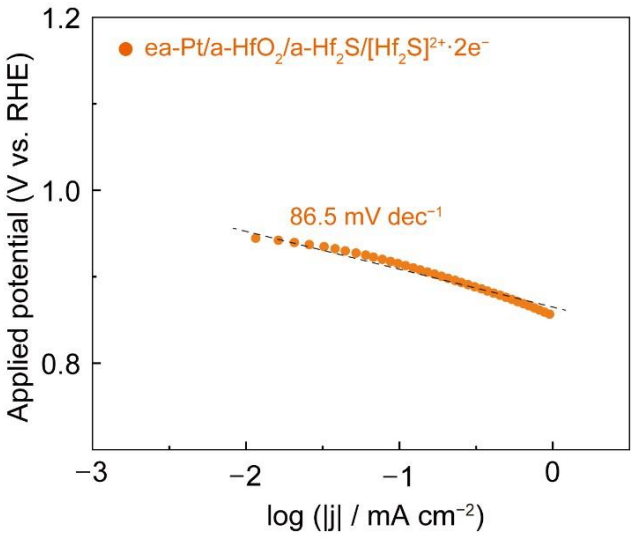

Fig. S21 Tafel plot for the ea-Pt/a-HfO_2/a-Hf_2S/$[Hf_2S]^{2+}$·$2e^-$. Tafel plot obtained from the ORR LSV polarization curve in Fig. S20.

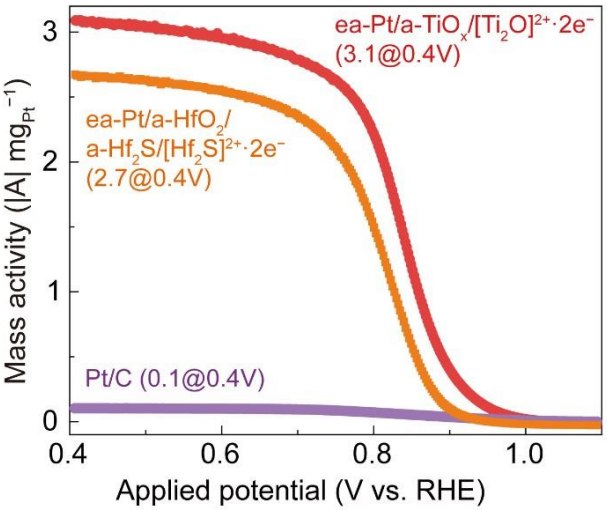

Fig. S22 ORR mass activity. Calculated mass activity of the ea-Pt/a-HfO_2/a-Hf_2S/$[Hf_2S]^{2+}$·$2e^-$ in comparision with commercial Pt/C and ea-Pt/a-TiO_x/$[Ti_2O]^{2+}$·$2e^-$ catalysts.

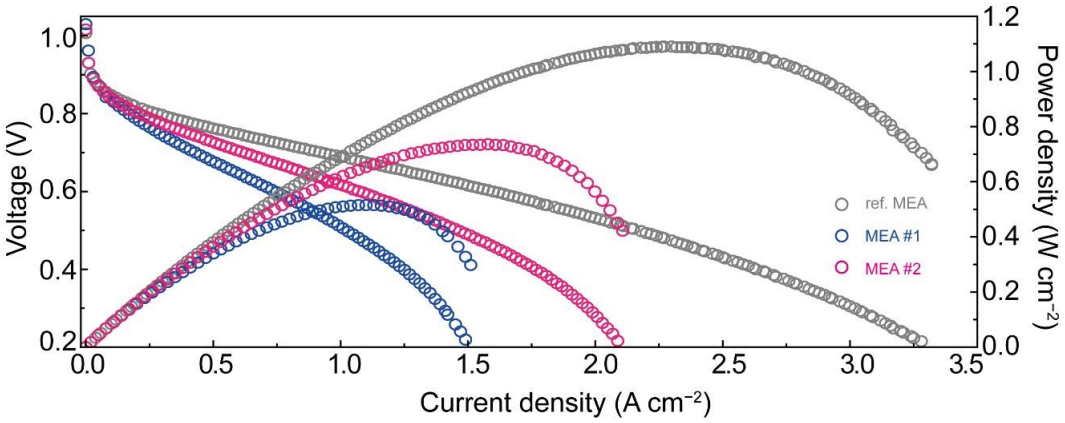

Fig. S23 Steady-state polarization plot of AEMFC fabricated by using ea-Pt/a-TiO_x/$[Ti_2O]^{2+}\cdot 2e^-$ as the cathode electrocatalyst.

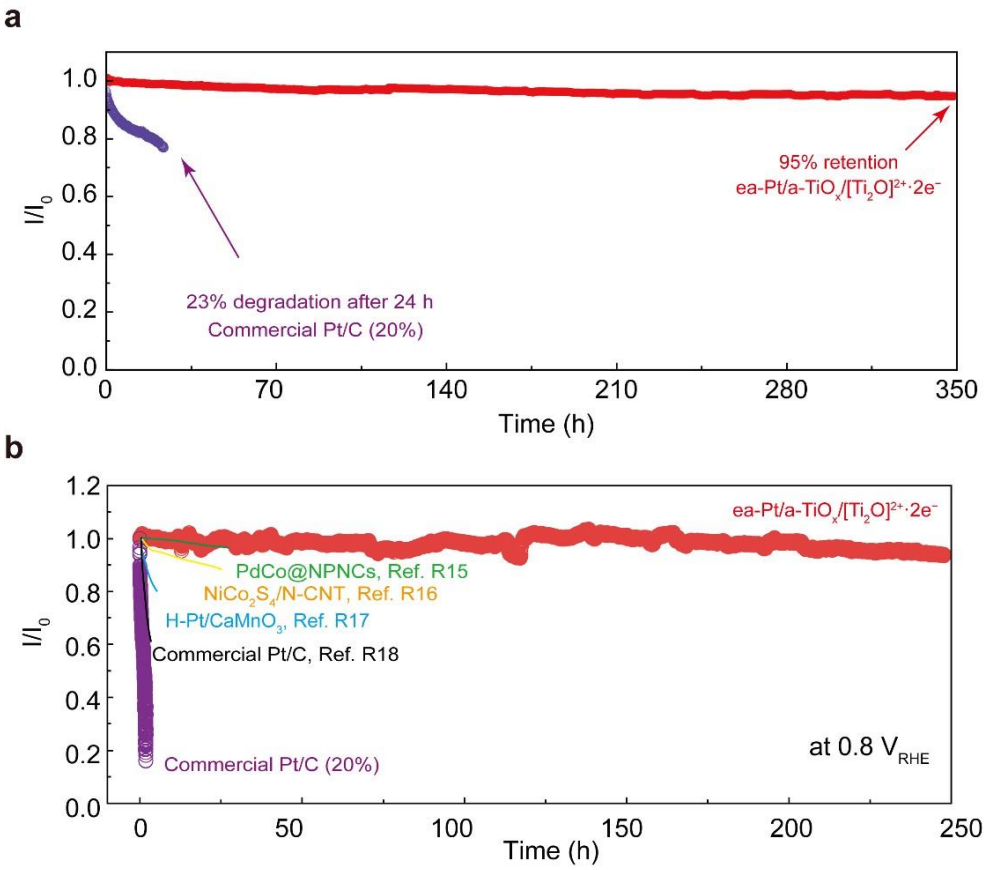

Fig. S24 Durability test of ea-Pt/a-TiO_x/$[Ti_2O]^{2+}$·$2e^-$ and the commercial Pt/C. (a) Durability test of ea-Pt/a-TiO_x/$[Ti_2O]^{2+}$·$2e^-$ at a constant applied potential of 0.4 V_{RHE}, which outperforms the durability of the commercial Pt/C. (b) Durability test of ea-Pt/a-TiO_x/$[Ti_2O]^{2+}$·$2e^-$ and the commercial Pt/C at a constant applied potential of 0.8 V_{RHE}, which outperforms the durability of the other catalysts that were evaluated in 0.1 M KOH solution at room temperature.

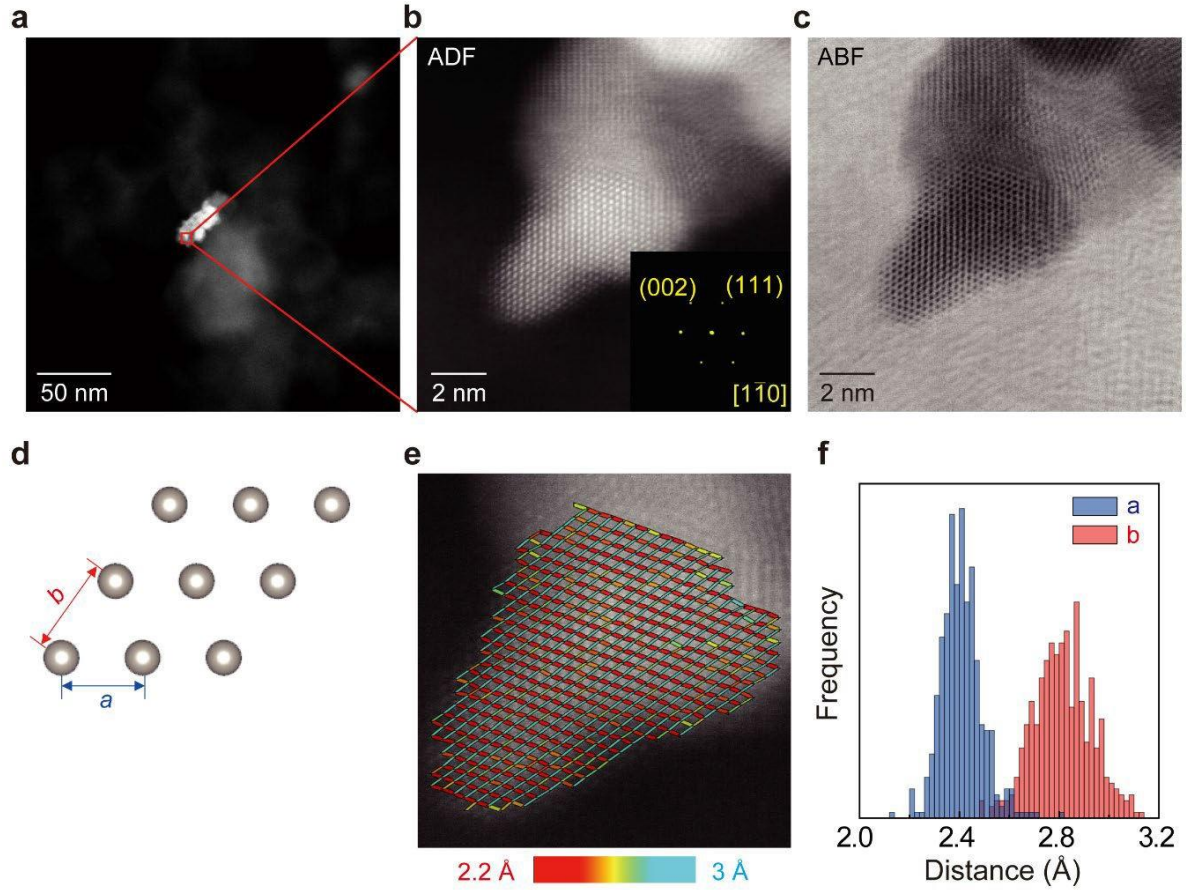

Fig. S25 Intact surface structure of Pt NP anchored on the a-TiO_x/$[Ti_2O]^{2+}$·$2e^-$ support after the ORR. (a), (b), (c) Low resolution STEM (a), annular dark-field STEM (b), and annular bright-field STEM (c) images of a Pt NP anchored on the a-TiO_x/$[Ti_2O]^{2+}$·$2e^-$ support after the ORR. (d) Atomic structure on (110) plane of metal Pt. (e) Projected atomic grids for the Pt NP anchored on the a-TiO_x/$[Ti_2O]^{2+}$·$2e^-$ support. (f) Distributions of atomic distance obtained by the projected atomic distance analysis for the grid region.

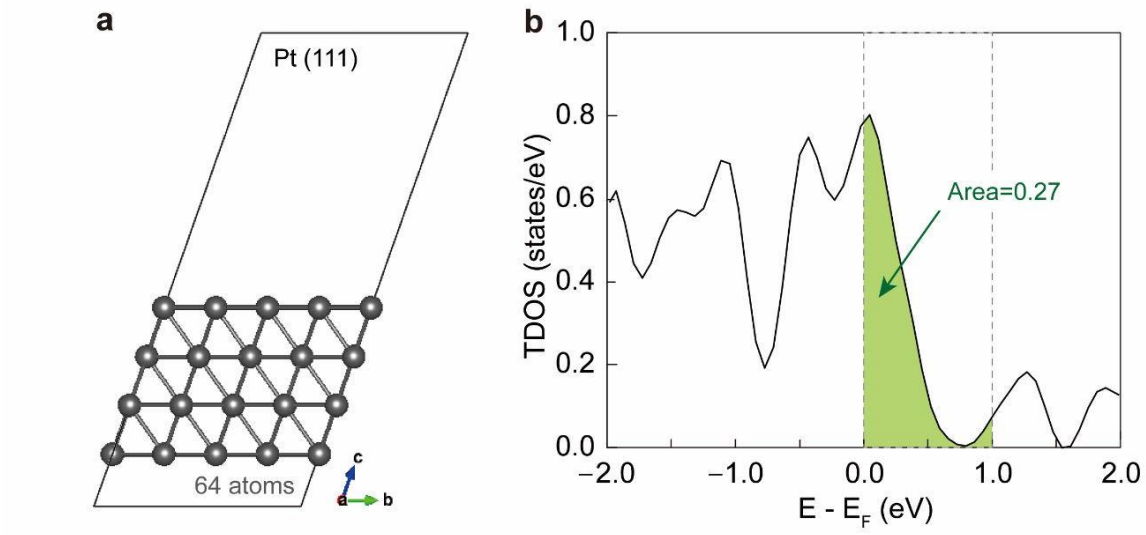

Fig. S26 Theoretical modeling of negatively charged Pt NPs. (a) Slab model of Pt (111). (b) Corresponding total density of state (TDOS) for the neutral Pt (111), which was represented by black line. From the difference between ϕ values of Pt metal and the negatively charged Pt NPs, which was set to be 1.0 eV, the number of excess electrons was extracted by the integral of the green area, which gives $0.27e^-$ per one Pt atom.

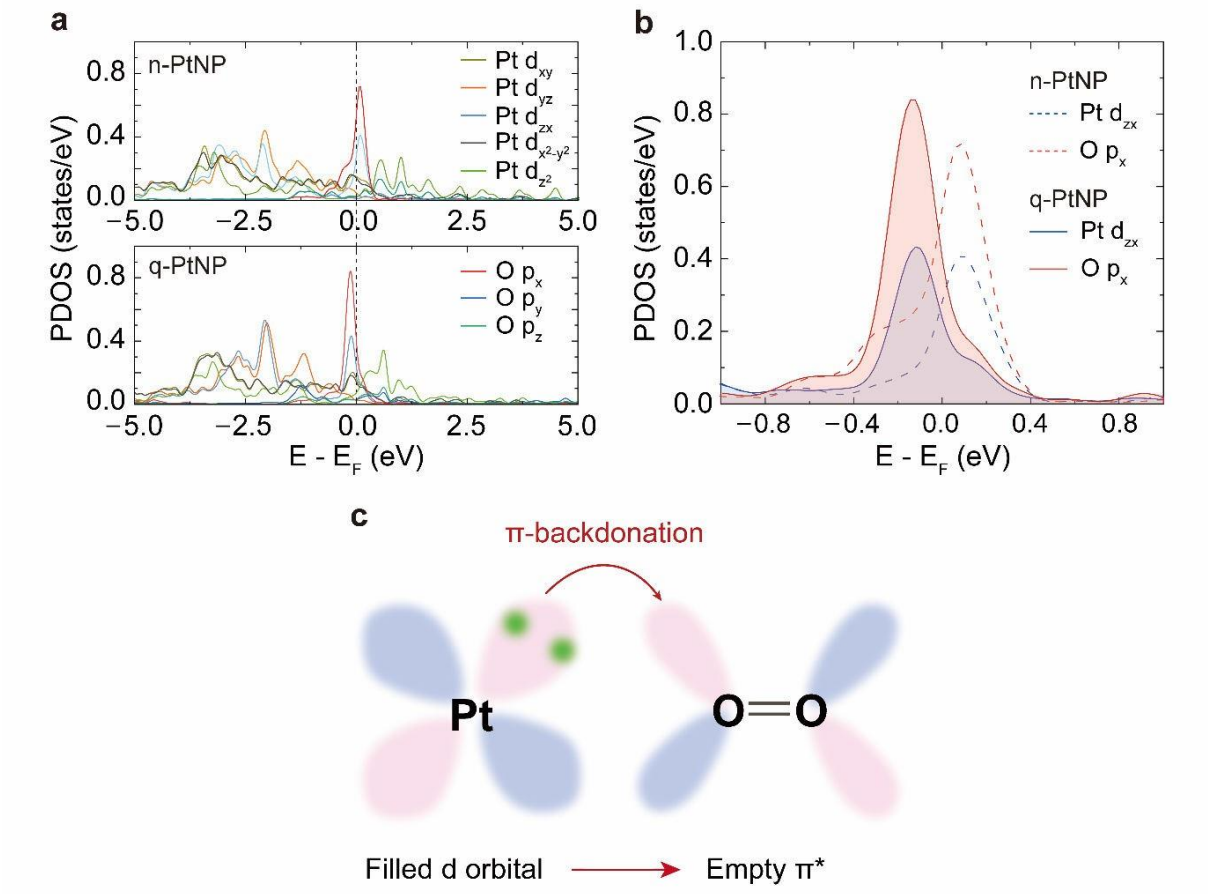

Fig. S27 Charge transfer of surface-accumulated excess electrons to adsorbed O atoms. (a) Partial density of state (PDOS) for the modelled neutral (n-PtNP) and negatively charged Pt (111) (q-PtNP). (b) Enlarged PDOS of Pt d_{zx} and O p_x orbitals near Fermi level. (c) Schematic illustration of the π-backdonation from Pt d_{zx} to O p_x orbitals.

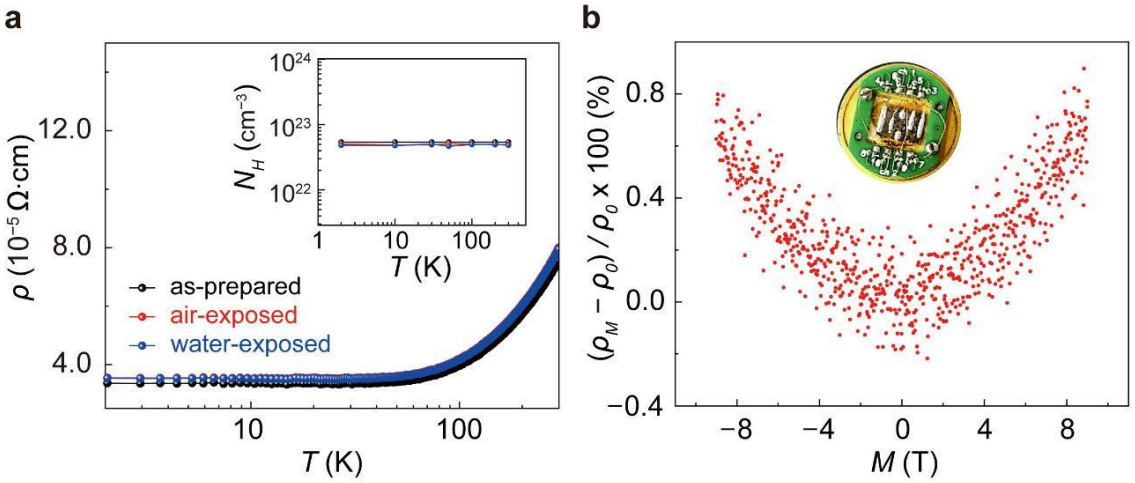

Fig. S28 Electrical transport properties of $[Ti_2O]^{2+}\cdot 2e^-$ electride. (a) Temperature dependence (T) of electrical resistivity (ρ) for the $[Ti_2O]^{2+}\cdot 2e^-$ electrides that were exposed to different atmospheres. (b) Magnetic field (M) dependence of magnetoresistance for the air-exposed $[Ti_2O]^{2+}\cdot 2e^-$ electride, showing the characteristics of metallic conduction. The inset of (a) showed the temperature dependent carrier concentration (N_H) with a negligible change.

Table S1 Structural parameters of Ti_2O crystal obtained by Rietveld refinement.

Crystal system	Hexagonal
Space group	$PP\bar{3}mm1$
Z	1
a (Å)	2.963043(43)
b (Å)	2.963043(43)
c (Å)	4.846344(51)
α (°)	90
β (°)	90
γ (°)	120
V ($Å^3$)	36.849
Ti position	(1/3, 2/3,0.267815)
O position	(0, 0, 0)
R_{wp} *(%)*	7.07
R_p *(%)*	5.26

Table S2 XPS results of the a-TiO_x/$[Ti_2O]^{2+}\cdot 2e^-$ samples. Peaks are calibrated with reference Au 4*f*.

Samples		Position (eV)	Area (a.u.)	Atomic percentage (%)
Ti^{4+} 2*p* (eV)/(at.%)	12h-Ar-sputtered	N.A.	N.A.	N.A.
	8h-Ar-sputtered	459.08	199.66	38.66
	Air-exposed	459.04	1048.61	76.78
Ti^{3+} 2*p* (eV)/(at.%)	12h-Ar-sputtered	457.35	30.74	1.79
	8h-Ar-sputtered	457.34	166.48	37.38
	Air-exposed	457.28	137.37	12.22
Ti^{2+} 2*p* (eV)/(at.%)	12h-Ar-sputtered	454.41	684.12	98.21
	8h-Ar-sputtered	454.63	109.22	23.96
	Air-exposed	454.59	103.75	11.00
O^{2-} 1*s* (eV)/(at.%)	12h-Ar-sputtered	530.78	143.00	43.23
		531.76	196.06	57.78
	8h-Ar-sputtered	530.85	256.36	42.15
		531.50	351.80	57.85
	Air-exposed	530.92	706.03	51.50
		531.55	665.02	48.50

Table S3 XPS results of the Pt/a-TiO_x/$[Ti_2O]^{2+}\cdot 2e^-$ and ea-Pt/a-TiO_x/$[Ti_2O]^{2+}\cdot 2e^-$. Peak poisitions of Pt 4*f* are calibrated with reference Au 4*f*.

Samples		Position (eV)	Area (a.u.)	Atomic percentage (%)
Pt^{4+} 4*f* (eV)/(at.%)	Pt/a-TiO_x/ $[Ti_2O]^{2+}\cdot 2e^-$	74.91	12307.04	33.75
	ea-Pt/a-TiO_x/ $[Ti_2O]^{2+}\cdot 2e^-$	N.A.	N.A.	N.A.
Pt^{2+} 4*f* (eV)/(at.%)	Pt/a-TiO_x/ $[Ti_2O]^{2+}\cdot 2e^-$	72.41	10291.60	28.22
	ea-Pt/a-TiO_x/ $[Ti_2O]^{2+}\cdot 2e^-$	72.13	1610.16	25.56
Pt^0 4*f* (eV)/(at.%)	Pt/a-TiO_x/ $[Ti_2O]^{2+}\cdot 2e^-$	70.83	13865.01	38.03
	ea-Pt/a-TiO_x/ $[Ti_2O]^{2+}\cdot 2e^-$	70.73	4689.42	74.44

Table S4 Quantitative analysis for ICP-OES result of the ea-Pt/a-TiO_x/$[Ti_2O]^{2+}\cdot 2e^-$.

	Ti	Pt
Relative amount (wt.%)	88.5	0.7

Table S5 The detailed compositions of ref. MEA, MEA #1 and MEA #2 with specific formulations of each catalyst ink.

MEA	ref. MEA	MEA #1	MEA #2
Catalyst	20 wt.% Pt/C (50mg)	0.7 wt.% ea-Pt/a-TiO_x/$[Ti_2O]^{2+}\cdot 2e^-$ (50 mg)	0.7 wt.% ea-Pt/a-TiO_x/$[Ti_2O]^{2+}\cdot 2e^-$ (25 mg) + Vulcan Carbon (25 mg)
DI Water	500 µL	500 µL	500 µL
IPA	2500 µL	2500 µL	2500 µL
Ionomer Solution (5 wt.% QPC-TMA)	320 mg (= 16 mg Ionomer)	380 mg (= 19 mg Ionomer)	390 mg (= 19.5 mg Ionomer)

Table S6 The detailed components of ref. MEA, MEA #1 and MEA #2.

MEA	ref. MEA	MEA #1	MEA #2
Anode PTL	Carbon Paper w/ MPL (JNT-30-A3)		
Anode	60 wt.% PtRu/C (0.4 mg_{PtRu} cm^{-2}) Ionomer = QPC-TMA		
Membrane	QPC-TMA (50 μL)		
Cathode	20 wt.% Pt/C (0.05 mg_{Pt} cm^{-2}) Ionomer = QPC-TMA	0.7 wt.% ea-Pt/a-TiO_x/$[Ti_2O]^{2+}$·$2e^-$ (0.01 mg_{Pt} cm^{-2}) Ionomer = QPC-TMA	0.7 wt.% ea-Pt/a-TiO_x/$[Ti_2O]^{2+}$·$2e^-$ (0.01 mg_{Pt} cm^{-2}) + Vulcan Carbon (1 mg_C cm^{-2}) Ionomer = QPC-TMA
Cathode PTL	Carbon Paper w/ MPL (JNT-30-A3)		

Table S7 Comparisons of the ORR performance both under the applied potential of 0.9 V_{RHE} and 0.4 V_{RHE} of recently published Pt nanostructure catalysts.

Catalyst	Electrolyte	Mass activity [a] (0.9 V_{RHE})	Mass activity [b] (0.4 V_{RHE})	Specific activity [a] (0.9 V_{RHE})	Specific activity [b] (0.4 V_{RHE})	ECSA	Reference
		$\lvert A \rvert\ mg_{Pt}^{-1}$	$\lvert A \rvert\ mg_{Pt}^{-1}$	$mA\ cm^{-2}$	$mA\ cm^{-2}$	$m^2\ g^{-1}$	
ea-Pt/ a-TiO_x/ $[Ti_2O]^{2+}$·2e⁻	**0.1 M KOH**	**0.45**	**3.1**	**2.1**	**14.2**	**21.7**	**This work**
Pt_3Fe NW	0.1 M $HClO_4$	2.11	1.23	4.34	2.53	34	*Adv. Mater.* **2018**, 30, 1705515
Ga-doped PtNi	0.1 M $HClO_4$	1.24	0.26	2.53	0.53	49	*Nano Lett.* **2018**, 18, 2450
PtNi frame	0.1 M $HClO_4$	1.51	0.17	2.05	0.23	73.4	*Nano Lett.* **2018**, 18, 2930
PtNi frame	0.1 M $HClO_4$	0.24	0.86	0.44	1.57	54.8	*ACS Nano* **2018**, 12, 8697
Pt cube	0.1 M $HClO_4$	0.43	0.62	1.77	2.56	24.5	*Mater. Today* **2018**, 21, 834
PtNiCo NW	0.1 M $HClO_4$	4.2	1.71	5.11	2.08	82.2	*Sci. Adv.* **2017**, 3, 1601705
Rh-Pt NW	0.1 M $HClO_4$	1.41	0.35	1.63	0.41	86.4	*J. Am. Chem. Soc.* **2017**, 139, 8152
PtPb/PtNi IM	0.1 M $HClO_4$	1.92	0.41	5.16	1.11	37.2	*J. Am. Chem. Soc.* **2017**, 139, 9576
PtNiPd NW	0.1 M $HClO_4$	1.93	0.57	3.48	1.03	55.4	*Adv. Mater.* **2017**, 29, 1603774
Pt_3Co NW	0.1 M $HClO_4$	3.71	0.91	7.12	1.75	52.1	*Nat. Commun.* **2016**, 7, 11850
Jagged Pt NW	0.1 M $HClO_4$	13.6	2.61	11.5	2.21	118	*Science* **2016**, 354, 1414
PtPb/Pt plate	0.1 M $HClO_4$	4.3	0.94	7.8	1.7	55.1	*Science* **2016**, 354, 1410
Mo-Pt_3Ni	0.1 M $HClO_4$	6.98	1.4	10.3	2.06	67.5	*Science* **2015**, 348, 1230
Pt Nanocage	0.1 M $HClO_4$	1.28	0.53	3.5	1.44	36.6	*Nano Lett.* **2016**, 16, 1467
Pt Nanocage	0.1 M $HClO_4$	0.75	0.45	1.98	1.19	38.2	*Science* **2015**, 349, 412
Pd@Pt NP	0.1 M $HClO_4$	1.6	0.73	1.66	0.76	96.4	*J. Am. Chem. Soc.* **2015**, 137, 15036
PtNi thin film	0.1 M $HClO_4$	0.216	0.09	2.4	1.01	9	*Nat. Mater.* **2012**, 11, 1051
Rh-PtNi	0.1 M $HClO_4$	1.14	0.36	-	-	-	*Nano Lett.* **2016**, 16, 1719

Pt Nanotube	0.1 M $HClO_4$	0.5	0.2	1.48	0.59	34.2	*J. Am. Chem. Soc.* **2016**, 138, 6332
PtNi-NiB NP	0.1 M $HClO_4$	5.3	0.91	9.05	1.55	59	*Nat. Commun.* **2016**, 7, 12362
Pt Nanocages	0.1 M $HClO_4$	1.12	0.34	2.48	0.76	45.2	*J. Am. Chem. Soc.* **2016**, 138, 1494
Pd@$Pt_{1.8}$Ni NP	0.1 M $HClO_4$	0.79	0.43	0.45	0.25	-	*J. Am. Chem. Soc.* **2015**, 137, 2804
PtCu OFAs	0.1 M $HClO_4$	3.26	0.76	5.98	1.39	54.5	*Adv. Mater.* **2017**, 29, 1601687
$L1_0$-CoPt/Pt	0.1 M $HClO_4$	2.26	0.25	8.26	0.92	27.3	*Joule* **2019**, 3, 124
LP@PF-2	0.1 M $HClO_4$	12.36	3.81	-	-	-	*Science* **2018**, 362, 1276
PtNi-BNCs	0.1 M $HClO_4$	3.52	1.28	5.16	1.88	68.2	*Science* **2019**, 366, 850
Pt/DPC	0.1 M $HClO_4$	-	0.07	1.76	5.84	-	*Electrocatalysis* **2020**, 11, 497
Pt/NGC	0.1 M $HClO_4$	-	0.08	-	-	-	*Adv. Energy Mater.* **2021**, 11, 2101050
$Pt_{4.8}$Fe/PCNF	0.1 M $HClO_4$	-	0.08	-	-	70.2	*Int. J. Hydrogen Energy* **2019**, 44, 18083
Pt/SnO_2-CNT	0.1 M $HClO_4$	0.07	0.19	0.25	0.67	-	*J. Electroanal. Chem.* **2021**, 896, 115147
Pt@NiNC	0.5 M H_2SO_4	0.03	0.2	0.03	0.19	102.9	*Catal. Sci. Technol.* **2020**, 10, 65
Pt/ CNF-1300-0.28Mn	0.1 M $HClO_4$	0.12	0.25	0.31	0.63	-	*New J. Chem.* **2021**, 45, 14608
M-$PtTe_2$	0.1 M KOH	0.2	0.26	-	-	-	*ACS Energy Lett.* **2021**, 6, 3481
Pt-TNT/FAB	0.1 M $HClO_4$	0.04	0.28	0.075	0.56	49.6	*Int. J. Hydrogen Energy* **2019**, 44, 4745
PtCM100-A900	0.1 M $HClO_4$	0.02	0.34	-	-	-	*ChemElectroChem* **2018**, 5, 62
Pt-Mn_3O_4/C	0.5 M H_2SO_4	0.18	0.35	0.08	0.16	135.3	*J. Electroanal. Chem.* **2017**, 794, 164

[a] The data was adapted from the Table. S1 in the reference *6*.

[b] The data is not given in the references, but excavated from the ORR polarization curves.

Table S8 Comparisons of the ORR performance under alkaline electrolyte at the applied potential of 0.9 V_{RHE} and 0.4 V_{RHE} of recently published Pt nanostructure catalysts.

Catalyst	Electrolyte	Mass activity (0.9 V_{RHE})	Mass activity (0.4 V_{RHE})	Specific activity (0.9 V_{RHE})	Specific activity (0.4 V_{RHE})	ECSA	Onset potential	Half-wave potential	Electron transfer number	Reference
		$\|A\| mg_{Pt}^{-1}$	$\|A\| mg_{Pt}^{-1}$	mA cm^{-2}	mA cm^{-2}	$m^2 g^{-1}$	V_{RHE}	V_{RHE}	N/A	
ea-Pt/ a-TiO_x/ $[Ti_2O]^{2+}$ ·$2e^-$	**0.1 M KOH**	**0.45**	**3.1**	**2.1**	**14.2**	**21.7**	**0.90**	**0.82**	**3.92~ 3.97**	**This work**
Ni-HIF Pt	0.1 M KOH	3.35	1.31	5.11	3.48	61.57	0.96	0.90	3.88~ 3.98	*Nano Energy* **2022**, 103, 107800
Pt aer-[MTBD][PFSI]	0.1 M KOH	0.581	0.16	0.881	0.34	65.9	1.024	0.934		*ACS Appl. Mater. Interfaces* **2023**, 15, 21143
Pt@N,F-HCS	0.1 M KOH	1.76	1.50	2.73	15.74	64.3	0.98	0.84	4.0	*J. Mater. Chem. A*, **2023**, 11, 4319
Pt-Ni-Ir yolk-shell	1 M KOH	0.391	0.18	0.961	0.77	42	0.97	0.918		*Nanoscale* **2019**, 11, 23206
Pt_3Ni/ CA	0.1 M KOH	0.25	0.042	0.469	0.084	59.1	0.98	0.94		*J. Solid State Electr.* **2022**, 26, 481
Pt-Cu-Mn UNFs	0.1 M KOH	1.45	0.49	3.38	1.73	43	0.96	0.92		*Adv. Funct. Mater.* **2020**, 30, 1910107
$Au_{1.68}Pt$/ MWNTs	0.1 M KOH	0.295	0.19	0.16	0.28	184.5	0.95	0.89	3.8~4.0	*Appl. Surf. Sci.* **2021**, 564, 150474
20Pt/ SGCN-550	0.1 M KOH	0.68	0.25	1.49	0.86	46.2		0.91	4.0	*ACS Catal.* **2022**, 12, 7406

References

1 C. T. Dinh, A. Jain, F. P. G. de Arquer, P. D. Luan, J. Li, N. Wang, X. Zheng, J. Cai, B. Z. Gregory, O. Voznyy, B. Zhang, M. Liu, D. Sinton, E. J. Crumlin and E. H. Sargent, *Nat. Energy*, 2019, **4**, 107–114.

2 B. Ravel and M. Newville, *J. Synchrotron Rad.*, 2005, **12**, 537–541.

3 L. Gao, T. Sun, X. Tan, M. Liu, F. Xue, B. Wang, J. Zhang, Y. F. Lu, C. Ma, H. Tian, S. Yang, S. C. Smith and H. Huang, *Appl. Catal., B*, 2022, **303**, 120918.

4 M. Luo and M. T. M. Koper, *Nat. Catal.*, 2022, **5**, 615–623.

5 L. Zhang, J. M. T. A. Fischer, Y. Jia, X. Yan, W. Xu. X. Wang, J. Chen, D. Yang, H. Liu, L. Zhuang, M. Hankel, D. J. Searles, K. Huang, S. Feng, C. L. Brown and X. Yao, *J. Am. Chem. Soc.*, 2018, **140**, 10757–10763.

6 H. Dong, J. Liang, Y. Wang, Z. Xu, Q. Liu, Y. Luo, T. Li, L. Li, X. Shi, A. M. Asiri, Q. Li, D. Ma, and X. Sun, *Angew. Chem. Int. Ed.*, 2021, **60**, 10583–10587.

7 Z. Yang, C. Zhao, Y. Qu, H. Zhou, F. Zhou, J. Wang, Y. Wu and Y. Li, *Adv. Mater.*, 2019, **31**, 1808043.

8 M. S. Cha, J. E. Park, S. Kim, S. H. Han, S. H. Shin, S. H. Yang, T. H. Kim, D. M. Yu, S. So, Y. T. Hong, S. J. Yoon, S. G. Oh, S. Y. Kang, O. H. Kim, H. S. Park, B. Bae, Y. E. Sung, Y. H. Cho and J. Y. Lee, *Energy Environ. Sci.*, 2020, **13**, 3633–3645.

9 G. Kresse and J. Furthmuller, *Comp. Mater. Sci.*, 1996, **6**, 15–50.

10 G. Kresse and J. Furthmuller, *Phys. Rev. B*, 1996, **54**, 11169–11186.

11 G. Kresse and D. Joubert, *Phys. Rev. B*, 1999, **59**, 1758–1775.

12 J. P. Perdew, K. Burke and M. Ernzerhof, *Phys. Rev. Lett.*, 1996, **77**, 3865–3868.

13 H. J. Monkhorst and J. D. Pack, *Phys. Rev. B*, 1976, **13**, 5188–5192.

14 K. Chung, J. Bang, A. Thacharon, H. Y. Song, S. H. Kang, W. S. Jang, N. Dhull, D. Thapa, C. M. Ajmal, B. Song, S. G. Lee, Z. Wang, A. Jetybayeva, S. Hong, K. H. Lee, E. J. Cho, S. Baik, S. H. Oh, Y. M. Kim, Y. H. Lee, S. G. Kim and S. W. Kim, *Nat. Nanotechnol.*, 2022, **17**, 285–291.

15 Z. Zhang, S. Liu, X. Tian, J. Wang, P. Xu, F. Xiao and S. Wang, *J. Mater. Chem. A*, 2017, **5**, 10876–10884.

16 X. Han, X. Wu, C. Zhong, Y. Deng, N. Zhao and W. Hu, *Nano Energy*, 2017, **31**, 541–550.

17 X. Han, F. Cheng, T. Zhang, J. Yang, Y. Hu and J. Chen, *Adv. Mater.*, 2014, **26**, 2047–2051.

18 Z. Hu, Z. Zhang, Z. Li, M. Dou and F. Wang, *ACS Appl. Mater. Interfaces*, 2017, **9**, 16109–16116.